The Astrophysical Journal Letters, 998:L16 (11pp), 2026 February 10 https://doi.org/10.3847/2041-8213/ae3c0a

A 2 au Resolution View by ALMA of the Planet-hosting WISPIT 2 Disk

Stefano Facchini[1], Pietro Curone[2], Myriam Benisty[3], Francesco Zagaria[3], Richard Teague[4], Gabriele Cugno[5], and Jaehan Bae[6]
[1] Dipartimento di Fisica, Università degli Studi di Milano, Via Celoria 16, 20133, Milano, Italy; stefano.facchini@unimi.it
[2] Departamento de Astronomía, Universidad de Chile, Camino El Observatorio 1515, Las Condes, Santiago, Chile
[3] Max-Planck Institute for Astronomy (MPIA), Königstuhl 17, 69117 Heidelberg, Germany
[4] Department of Earth, Atmospheric, and Planetary Sciences, Massachusetts Institute of Technology, Cambridge, MA 02139, USA
[5] Department of Astrophysics, University of Zürich, Winterthurerstrasse 190, 8057 Zürich, Switzerland
[6] Department of Astronomy, University of Florida, Gainesville, FL 32611, USA
Received 2025 December 8; revised 2026 January 12; accepted 2026 January 22; published 2026 February 5

Abstract

We present deep, high-spatial-resolution interferometric observations of 0.88 mm continuum emission from the TYC 5709-354-1 system, hereafter WISPIT 2, obtained with the goal of detecting circumplanetary emission in the vicinity of the newly discovered WISPIT 2b planet. Observations with the most extended baseline configuration offered by the Atacama Large Millimeter/submillimeter Array, achieving an angular resolution of 25 × 17 mas (3.3 × 2.2 au), revealed a single, narrow ring with a deprojected radius of 144.4 au and width of 7.2 au, and no evidence of circumplanetary emission within the cavity. Injection and recovery tests demonstrate that these observations can rule out pointlike emission at the location of WISPIT 2b brighter than ≈45 μJy at the 3σ level. While these data can rule out PDS 70 c-like circumplanetary emission, the upper limit is consistent with empirical mass–flux relationships extrapolated from the stellar regime. Visibility modeling of the continuum ring confirms that WISPIT 2b lies significantly interior to the millimeter dust ring, raising doubts about the ability of WISPIT 2b to be the only driver of the dust structure. Possible solutions include either another lower-mass companion, residing between WISPIT 2b and the cavity edge, likely in the gap seen by SPHERE at ∼130 au, or that WISPIT 2b is either substantially more massive than estimates based on IR photometry (∼15 $M_{\rm Jup}$) or on a moderately eccentric orbit. The combination of observations sensitive to the gas and dust distributions on larger spatial scales and dedicated hydrodynamical modeling will help differentiate between scenarios.

Unified Astronomy Thesaurus concepts: Protoplanetary disks (1300); Planet formation (1241); Radio interferometry (1346)

1. Introduction

Planet–disk interactions are widely considered as a likely origin of the substructures routinely revealed in high-resolution observations from the Atacama Large Millimeter/submillimeter Array (ALMA) in the submillimeter regime (e.g., S. M. Andrews 2020) and from infrared scattered-light instruments (e.g., M. Benisty et al. 2023). The most common substructures—rings and gaps—have often been attributed to unseen, embedded giant planets that carve dust-depleted gaps and create dust traps at the pressure maxima outside their orbits (e.g., P. Pinilla et al. 2012). While additional physical mechanisms (e.g., hydrodynamical instabilities) can produce annular substructures in disks, when applied to the population of observed rings and gaps, the planet interpretation would imply a large, yet-undetected population of giant planets at large separations (J. Bae et al. 2023; A. Ruzza et al. 2025). However, the search for protoplanets has been challenging, with many nondetections reported with direct imaging campaigns using both ground-based and space-based instruments (e.g., N. Huélamo et al. 2022; G. Cugno et al. 2023; B. B. Ren et al. 2023), possibly due to the circumstellar and circumplanetary disk material shielding the planet's thermal emission (G. Cugno et al. 2025).

Until recently, only PDS 70 b and c, two giant planets detected within a common dust-depleted cavity surrounded by a double-peaked ring, provided a clear case of accreting protoplanets still embedded in a gas-rich disk (M. Keppler et al. 2018; S. Y. Haffert et al. 2019; A. Isella et al. 2019; M. Benisty et al. 2021). However, recent multiepoch, multi-wavelength observations in different infrared (IR) bands (H, K, and L') and in the narrow Hα band unveiled a new protoplanet, WISPIT 2b (L. M. Close et al. 2025a; R. F. van Capelleveen et al. 2025). This planet is embedded in a protoplanetary disk surrounding a ∼1.08 $M_\odot$ star at a distance of 133 pc (R. F. van Capelleveen et al. 2025), and located at a separation of 0.″32 (57 au from the astrometric fitting) from the central star. Assuming an age of $5.1^{+1.3}_{-2.0}$ Myr, the measured H- and K_s-band infrared photometry by VLT/SPHERE led to an estimate of the planet mass of $4.9^{+0.6}_{-0.9}$ $M_{\rm Jup}$ (R. F. van Capelleveen et al. 2025). A consistent planet mass of 5.3 ± 1.0 $M_{\rm Jup}$ was obtained from L'-band photometry with LBT/LMIRcam by L. M. Close et al. (2025a). Unlike the two PDS 70 planets, which orbit within a common wide cavity (M. Keppler et al. 2019), WISPIT 2b appears to reside within a gap, surrounded by two rings of small dust grains seen in scattered light. The detection in the Hα filter by Magellan/MagAO-X (L. M. Close et al. 2025a) indicates that the planet is still accreting gas from its host protoplanetary disk at a rate of $2.25^{+3.75}_{-0.17} \times 10^{-12}$ $M_\odot$ yr^{-1}.

Although the exact dynamical and physical structure of the gas in the immediate vicinity of protoplanets remains uncertain

(e.g., E. Lega et al. 2024), it is generally thought that accretion onto a young planet is mediated by a circumplanetary disk (CPD; e.g., Y. Aoyama et al. 2018; G.-D. Marleau et al. 2023), which may also trap dust particles growing into satellitesimals (K. Batygin & A. Morbidelli 2020). In the PDS 70 system, millimeter continuum emission has been detected near both planets (A. Isella et al. 2019; M. Benisty et al. 2021; D. Fasano et al. 2025), possibly indicating the presence of dust grains trapped in a CPD, although multiwavelength observations of the material colocated with PDS 70 c may indicate a contribution from nonthermal emission (O. Domínguez-Jamett et al. 2025). The WISPIT 2b discovery now offers an additional laboratory in which to directly constrain planet–disk interactions, including dust trapping beyond the orbit of the planet, and to search for any circumplanetary material in the vicinity of the accreting protoplanet.

In this Letter, we examine the spatial distribution of dust continuum emission in the WISPIT 2 system using high-angular-resolution ALMA observations. The Letter is organized as follows: Section 2 describes the observational setup and data reduction; Section 3 presents the analysis of the dust continuum morphology and the search for CPDs; Section 4 discusses our findings; and Section 5 provides a summary and our conclusions.

2. Observations and Data Reduction

WISPIT 2 was observed with ALMA in Band 7 in the most extended C-10 configuration as part of the Director's Discretionary Time (DDT) program 2024.A.00064.S (PI Facchini). The current dataset comprises three back-to-back execution blocks obtained on 2025 September 10 for a total on-source integration time of 125 minutes. The wide hour-angle coverage results in excellent *uv* sampling for this configuration. Additional observations providing intermediate and short baselines are expected by summer 2026.

Band 7 was chosen as it offers the optimal trade-off between sensitivity and observing efficiency necessary to achieve the required detection significance. This choice was made assuming that the spectral index of the CPD around WISPIT 2b is comparable to that of PDS 70 c, i.e., $\alpha = 2.0 \pm 0.2$ between Band 4 and Band 7 (O. Domínguez-Jamett et al. 2025; D. Fasano et al. 2025). Higher and lower frequency Bands were excluded due to the correspondingly longer integration times needed.

The observations were carried out under excellent atmospheric conditions, with precipitable water vapor between 0.25 and 0.4 mm, leading to a high execution fraction (capped at 1.5 following standard ALMA procedures). Baselines span 132–15,238 m across 47 antennas, yielding a maximum recoverable scale of $0\farcs27$ (substantially smaller than the $\gtrsim 2''$ diameter of the disk). Automated calibration was performed by ALMA staff, using J1912−0804 as phase calibrator and J1912−2914 for amplitude and bandpass calibration. The spectral setup consists of four frequency division mode windows with 3840 channels each (no online averaging), providing a total continuum bandwidth of 7.5 GHz. The central rest frequencies (LSRK) are 334.7, 336.6, 346.6, and 348.5 GHz. The lowest-frequency window exhibits an anomalously high phase rms compared to the others, but dedicated tests show that this does not impact the image quality.

The substantial spatial filtering arising from the extended configuration prevented effective self-calibration. We tested conservative phase-only self-calibration using models derived either from a `CLEAN` image or from the best-fit parametric disk model (Section 3.1); in both cases, the procedure failed to reduce imaging artifacts, since they are dominated by spatial filtering. Amplitude self-calibration was not attempted because the lack of short spacings compromises the derivation of reliable low-spatial-frequency amplitude gains. The upcoming data from shorter baselines will allow this approach.

For imaging preparation, we first flagged channels associated with expected bright lines (^{12}CO $J = 3$–2, SO 9_8–8_7, C_2H $N = 4$–3) and binned the remaining data into 62.5 MHz channels. Continuum images were produced using Briggs weighting with a range of robust parameters and *uv*-tapers, at a weighted frequency of 341.6 GHz. All reconstructions show nonnegligible artifacts induced by spatial filtering, including pronounced north–south ripples that elevate the rms within the central cavity of the ringlike structure. However, while the addition of shorter spacings will substantially improve imaging fidelity, the present dataset already enables robust scientific interpretation, in particular for point-source detection.

Our fiducial image adopts a Briggs `robust` parameter of 1.0, pixel size of $0\farcs0025$ ($\approx 1/8$ of the beam minor axis), multiscale `CLEAN`ing with scales [0, 7, 21, 35] (with the maximum scale covering the width of the ring), and a threshold of 42 μJy. Results are consistent across alternative imaging choices, including significant *uv*-tapers aimed at enhancing sensitivity to diffuse emission. The `CLEAN` mask traces a projected circular region of radius $1\farcs5$, inclined by 44° with a position angle (PA) of 359° (R. F. van Capelleveen et al. 2025). The rms measured within a projected circle of radius $0\farcs8$ is 16.6 μJy, approximately 1.5× the expected thermal noise, indicating phase noise and imaging systematics. The synthesized beam of the fiducial image is 24 × 17 mas (3.3 × 2.2 au), PA = $57\fdg6$.

3. Results

The ALMA image of WISPIT 2 (Figure 1) shows a prominent thin ring at a distance of $1\farcs086$. With the selection of baselines available, no additional radial structure is observable in these data. The millimeter cavity is extremely wide, being one of the largest millimeter cavities observed to date (e.g., N. van der Marel 2023). However, we caution the reader not to overinterpret the reconstructed image for three main reasons: (1) we are not sensitive to emission with spatial scales $\gtrsim 0\farcs27$ (we are effectively imaging a high-pass-filter intensity map); (2) the extremely high angular resolution limits the sensitivity to low-surface-brightness emission; (3) imaging artifacts induce azimuthal variations in the emission of the millimeter ring. This third effect is particularly clear in the large negative emission at PA ∼ 45° and ∼225° in the inner cavity (see Figure 2). However, it is possible that large-scale azimuthal modulations are present in the data but are filtered out in the C-10 array configuration. No emission (thermal or not) is seen at the center of the disk, thus we cannot conclude where the true position of the star is.

3.1. Parametric Model of the Submillimeter Ring

In order to better reconstruct the emission of the WISPIT 2 ring given the limited *uv* coverage, we model the visibility data with a single, circular, thin Gaussian ring, with the intensity

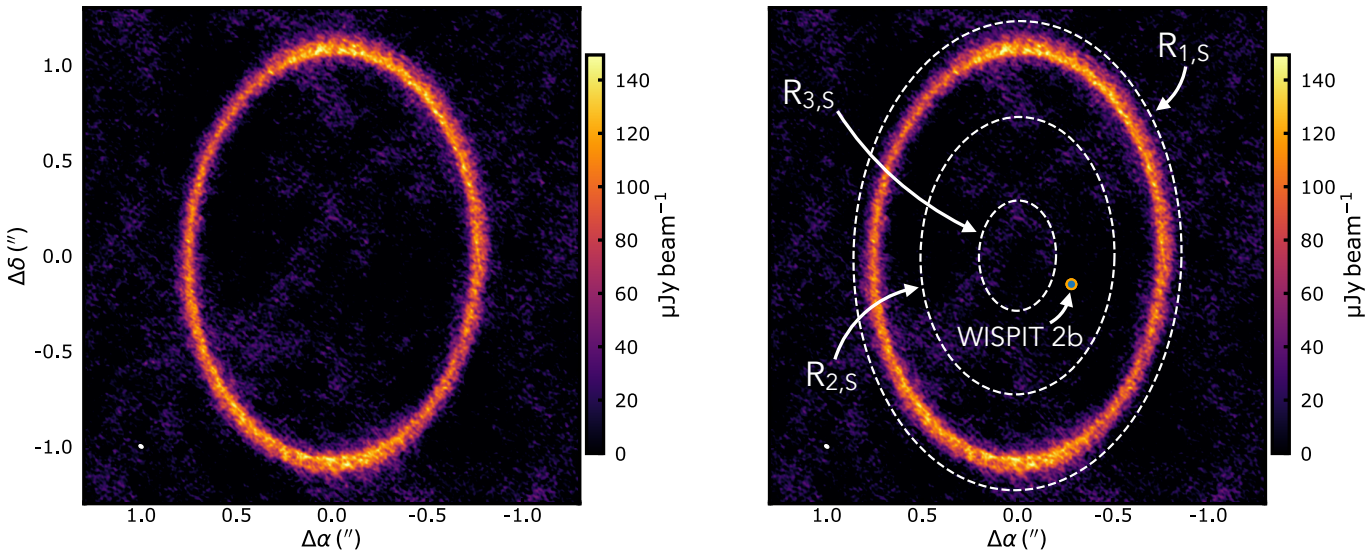

Figure 1. 0.88 mm continuum intensity of the WISPIT 2 system, showing a thin ring at 1.″086 (144.4 au deprojected distance). The right panel shows the same image, with white dashed lines indicating the radial peaks observed in IR scattered light by R. F. van Capelleveen et al. (2025), projected onto the disk midplane. The numbering ($R_{N,S}$) follows that by R. F. van Capelleveen et al. (2025). The location of the WISPIT 2b planet (L. M. Close et al. 2025a; R. F. van Capelleveen et al. 2025) is highlighted in the right panel. The ALMA resolution element is shown at the bottom left of each panel.

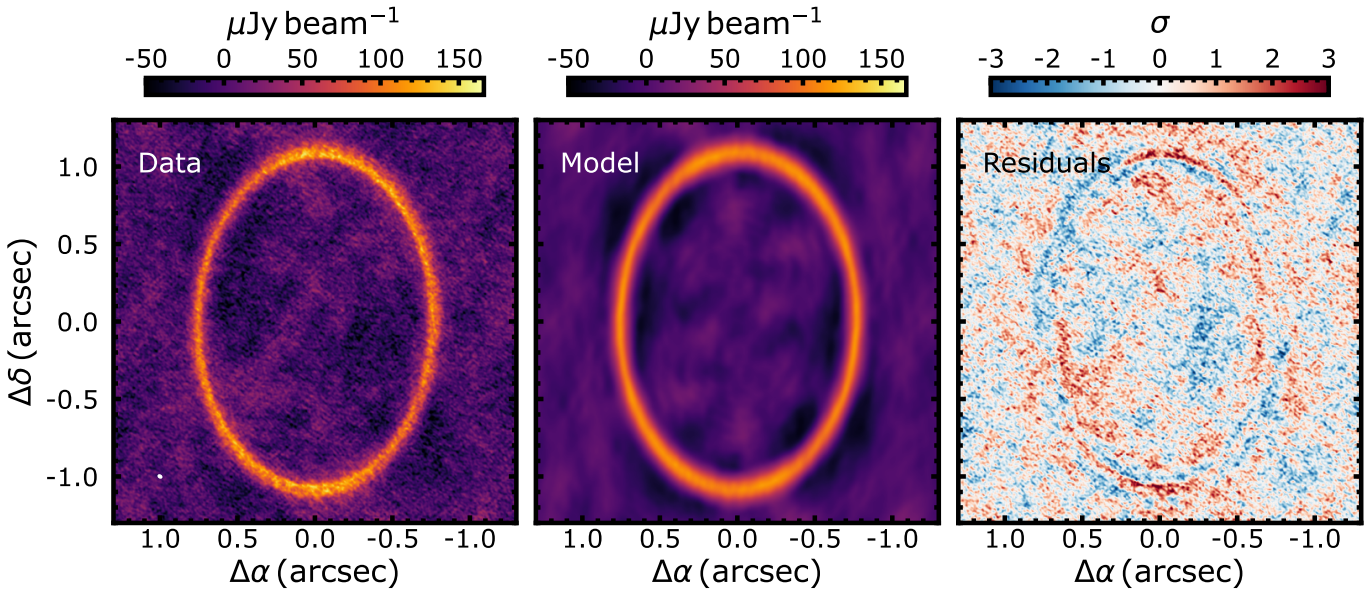

Figure 2. Data, best-fit `galario` model, and residuals of WISPIT 2. The intensity maps of both the model and the residuals have been reconstructed with the same `CLEAN`ing parameters as the original data. The rms ($\sigma = 16.6$ μJy) used in the residuals color bar is the one estimated within the millimeter cavity on the data (see Section 2).

described by

$$I(R) = I_0 \exp\left(\frac{-(R - R_{\rm ring})^2}{2\sigma_R^2}\right), \quad (1)$$

with R being the radius in cylindrical disk coordinates. The model is Fourier-transformed and sampled at the same uv-points as the observations using the `galario` code (M. Tazzari et al. 2018). The fit includes I_0, $R_{\rm ring}$, and σ_R as free parameters, together with the geometrical parameters defining the disk center (ΔR.A., ΔDecl.), the disk inclination (i), and its position angle (PA). . The best-fit model is obtained by exploring the likelihood with the `emcee` package (D. Foreman-Mackey et al. 2013), with 100 walkers and 18,000 steps, after a burn-in of 8000 steps. The fit converges well to a radially resolved thin ring peaked at 1.″086 (144.4 au), with a width $\sigma_R = 0.''054$ (7.2 au). The uncertainties and additional best-fit values are reported in Table 1, where uncertainties neglect the systematics associated with the inflexibility of the parametric model. The retrieved inclination and position angle are in agreement with the values obtained in the H band and K_S band (R. F. van Capelleveen et al. 2025), which were also obtained under the assumption of circular morphology of the emission. The match in inclination and position angle between

Table 1
Best-fit Parameters of the Gaussian-ring `Galario` Model of WISPIT 2

I_0 (Jy sr^{-2})	$R_{\rm ring}$ (arcsec)	σ_R (arcsec)	i (deg)	PA (deg)	ΔR.A. (mas)	ΔDecl. (mas)
$9.996^{+0.001}_{-0.001}$	$1.08613^{+0.00001}_{-0.00001}$	$0.0544^{+0.0001}_{-0.0001}$	$45.6608^{+0.0005}_{-0.0003}$	$178.6396^{+0.0004}_{-0.0005}$	$-4.1^{+0.1}_{-0.1}$	$-1.7^{+0.1}_{-0.1}$

Note. Uncertainties are computed from the 16th and 84th percentiles of the marginalized posterior distributions. The displacements of the center of the annulus are relative to the absolute International Celestial Reference System coordinates $19^{\rm h}23^{\rm m}17\overset{\rm s}{.}043704$, $-07°40'55\overset{''}{.}77275$.

the IR and ALMA data indicates that a comparable level of eccentricity would be present in the two datasets. Both the model and residual visibilities are imaged as the original data (Figure 2), with the residuals showing low significance but structured residual patterns ($\lesssim 3\sigma$), indicating that a Gaussian representation is not perfect. The best-fit model yields a total disk flux density of 151.4 ± 0.3 mJy, where the uncertainty represents the 16th and 84th percentiles of the total flux density distribution derived from the last 1000 model iterations. The azimuthally averaged, deprojected visibilities and the best-fit `galario` model are shown in Appendix A.

3.2. CPD Injection–Recovery

We search for any unresolved emission at the location of the WISPIT 2b planet to identify potential thermal or nonthermal radiation associated with the planet or its circumplanetary disk. Several approaches have been used in the literature to isolate compact CPD emission (e.g., A. Isella et al. 2019; M. Benisty et al. 2021; S. M. Andrews et al. 2021). In our data, however, inspection of the residual images after subtracting the `galario` best-fit model reveals no significant emission at the position of WISPIT 2b, regardless of the chosen imaging parameters.

To derive an upper limit on the CPD flux density, we must account for imaging artifacts introduced by spatial filtering, manifesting as correlated noise and large-scale ripples across the reconstructed images. We therefore adopt an injection–recovery methodology following S. M. Andrews et al. (2021). Specifically, we subtract the best-fit `galario` model from the visibilities and then inject a point source in visibility space at the location of the planet reported by R. F. van Capelleveen et al. (2025) ($r = 0\overset{''}{.}320$, PA $= 242\overset{\circ}{.}1$). The injection is implemented by modifying the publicly available scripts of S. M. Andrews et al. (2021). We then reimage the data using `CLEAN` parameters optimized to minimize the rms within the large cavity, which are the same as for the fiducial image. The recovered peak intensity is measured within an elliptical region centered on the injected source and with semiaxes 1.5 times the `CLEAN` beam.

We repeat this procedure for a number of CPD flux densities ranging from 10 to 200 μJy. Figure 3 shows the corresponding recovered flux densities, while in Appendix B we report images of the injection–recovery tests for CPD fluxes of 20, 50, and 80 μJy. The uncertainty on the CPD flux density is taken as the rms in the cavity of the residual image prior to any injection, which is 14.8 μJy (note that this is lower than the 16.6 μJy computed on the full data). This yields a 5σ upper limit of 75 μJy (or 45 μJy at 3σ) for a point-source CPD. This limit will improve as shorter baselines become available, enhancing image fidelity and point-source sensitivity. Finally, we emphasize that this constraint applies only to point-source

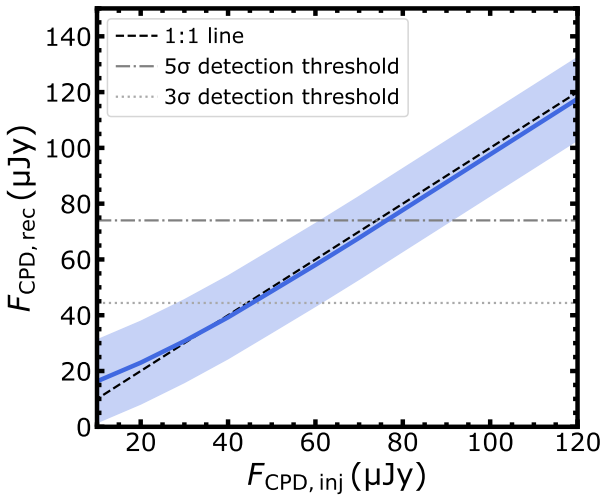

Figure 3. Injected ($F_{\rm CPD,inj}$) versus recovered ($F_{\rm CPD,rec}$) flux density of a point source at the location of WISPIT 2b. The recovered flux density is estimated as the peak intensity within 1.5 beams at that location. The ribbon indicates the 1σ uncertainty on the estimate of peak intensity.

emission; any spatially resolved CPD would exhibit lower surface brightness and could therefore remain undetected under these conditions (see Section 4.1).

With the same approach, we also search for any point-source emission colocated with the companion candidate CC 1 by L. M. Close et al. (2025a), at 15 au deprojected distance from the central star ($r = 0\overset{''}{.}110$, PA $= 192°$ in sky coordinates). No point source is seen in the data. The results of the injection–recovery procedure for CC 1 are shown in Appendix B.

4. Discussion

4.1. Interpreting the CPD Detection Limits

Although a nondetection, the excellent sensitivity achieved with these observations allows us to place meaningful constraints on the properties of the CPD. If the emission is assumed to be optically thin, then the upper limit on the flux density provides stringent upper limits on the total mass of the CPD, while for optically thick emission that same upper limit would yield a maximum radius of the CPD. In both cases, a CPD temperature, weighted by surface area, is needed. We use the same temperature as the one assumed for PDS 70 c, i.e., 26 K (M. Benisty et al. 2021), in order to allow a direct comparison with the only CPD detection in millimeter continuum known to date. Under the optically thin assumption, we use two different opacities to estimate the upper limit on the CPD dust mass, representing two scenarios for the dominant grain sizes (T. Birnstiel et al. 2018): 3.50 cm^2 g^{-1} for 1 mm-sized grains, and 0.76 cm^2 g^{-1} for 1 μm-sized grains. Using the full Planck law, the 5σ upper limit on the CPD flux

density yields an upper limit of $0.0090\,M_{\oplus}$ ($0.73\,M_{\rm Moon}$) and $0.0416\,M_{\oplus}$ ($3.38\,M_{\rm Moon}$) assuming millimeter-sized or micron-sized grains, respectively.

Similarly, we can estimate an upper limit on the size of the CPD, with the assumption of optically thick emission over the full extent of the disk. Using the same temperature as for the optically thin case (26 K), the upper limit on the CPD flux density relates to an upper limit on the millimeter radius of the CPD, with the following relation:

$$R_{\rm CPD} = \sqrt{\frac{d^2 F_{\rm CPD}}{\pi B_{\nu}(T)\cos i}}, \quad (2)$$

where d is the distance of the WISPIT 2 system (133 pc, R. F. van Capelleveen et al. 2025), $B_{\nu}(T)$ the Planck function, $F_{\rm CPD}$ the CPD flux density, and i the inclination of the CPD, assumed to be the same as for the circumstellar disk. The 5σ upper limit on the CPD flux density provides an upper limit on $R_{\rm CPD}$ of 0.62 au. This is smaller than the size of the CPD expected from a dynamical perspective, from which the size in gas of a CPD can be estimated as one-third of the Hill radius (e.g., B. A. Ayliffe & M. R. Bate 2009). By using a stellar mass of $1.08^{+0.06}_{-0.17}\,M_{\odot}$ and a mass for WISPIT 2b of $4.9^{+0.9}_{-0.6}\,M_{\rm Jup}$ (R. F. van Capelleveen et al. 2025), a Monte Carlo sampling of the two masses with asymmetric Gaussian distributions yields an expected radius for the CPD in gas of $R_{\rm gas,exp} = 2.07^{+0.13}_{-0.12}$ au. We can therefore exclude the presence of an optically thick CPD, with an extent of the continuum emission that is as large as one-third of the Hill radius. The same result was obtained by A. Isella et al. (2019) for PDS 70 c.

Given the exceptionally high angular resolution of our ALMA observations, a CPD with a radius equal to one-third of the Hill radius would be spatially resolved in our fiducial images, causing its emission to be distributed over multiple resolution elements. For completeness, we thus calculated the rms within the cavity of the residuals using progressively larger `CLEAN` beams in the image reconstruction. The corresponding rms scaling is presented in Appendix B.

4.2. Comparing the Millimeter Flux Density of WISPIT 2b with Other Systems

In Figure 4 we place our (3σ) upper limit on flux density in an empirical context by comparing it with the distribution of circumstellar and circumplanetary (sub)millimeter flux density versus host mass (as similarly shown by Y.-L. Wu et al. 2020; S. M. Andrews et al. 2021). Flux densities have been rescaled to a common frequency of 240 GHz with a spectral index $\alpha = 2.2$ for circumstellar disks (taken as the average of the 0.9–1.3 mm spectral indices of circumstellar disks, S. M. Andrews 2020) and 2.0 for circumplanetary emission (using the case of PDS 70 c as the only available benchmark, D. Fasano et al. 2025; O. Domínguez-Jamett et al. 2025), and to a distance of 150 pc. Dots and down-pointing arrows indicate millimeter continuum detections and 3σ upper limits, respectively. Circumstellar disks in nearby low-mass star formation regions (from the catalog of C. F. Manara et al. 2023) are shown as gray dots. The black dashed line indicates their best-fit linear correlation (with slope $\beta = 1.43 \pm 0.10$ and intercept $\alpha = 1.37 \pm 0.06$) obtained using the linear regression method implemented in `linmix` (B. C. Kelly 2007); single-chain

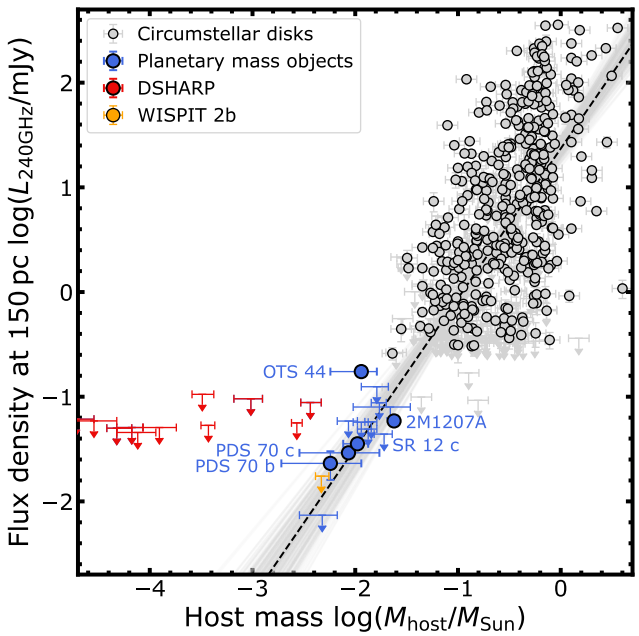

Figure 4. Distribution of circumstellar and circumplanetary flux density (rescaled to 240 GHz and 150 pc) as a function of the host mass. Most planetary-mass objects closely follow the trend (best-fit linear correlation, black dashed line) expected for circumstellar disks.

realizations are also shown (as lighter gray lines) to give a sense of the scatter around the best-fit curve. Overplotted in blue are the results of similar searches for (sub)millimeter continuum emission around low/planetary-mass companions in GSC 6214-210 B (B. P. Bowler et al. 2015), GQ Lup (M. A. MacGregor et al. 2017), 2MASS J12073346-3932539 A and B (2M1207, L. Ricci et al. 2017), SR 12 c (Y.-L. Wu et al. 2022), the sample of Y.-L. Wu et al. (2020), the isolated planetary-mass object OTS 44 (A. Bayo et al. 2017), and the planets PDS 70 c (M. Benisty et al. 2021; D. Fasano et al. 2025) and b (although potentially still contaminated by inner disk emission, D. Fasano et al. 2025). The masses of PDS 70 b and c were obtained from astrometric constraints by D. Trevascus et al. (2025), where we considered the large uncertainties they provide to be compatible with photometry-based masses (J. J. Wang et al. 2020). Finally, upper limits on the circumplanetary emission around the protoplanets proposed to be carving (some of) the DSHARP gaps, defined as the flux densities corresponding to a recovery fraction of at least 50% (S. M. Andrews et al. 2021), are also displayed in red (for the most recent estimates of planet masses by A. Ruzza et al. 2025). Our 3σ upper limit on (sub)millimeter continuum emission toward WISPIT 2b is shown as a yellow arrow. As noted by Y.-L. Wu et al. (2020) and S. M. Andrews et al. (2021), low-mass objects in the brown dwarf and planetary regime have flux densities well in line with those expected from a blind extrapolation of the correlation in place among circumstellar disks. The nondetection of a millimeter point source colocated with WISPIT 2b is consistent with this empirical correlation. However, the large scatter around the best-fit relation for circumstellar disks, combined with both the low flux densities expected from circumplanetary emission and the small number of detections, makes it extremely challenging to determine whether a different correlation applies to circumplanetary disks.

It is also meaningful to directly compare these results with the millimeter flux density measured for PDS 70 c, on the assumption that scalings of flux densities of CPDs deviate from the trend found for objects of stellar and brown dwarf mass, since the formation pathways of their disks are expected to be very different. Under the assumption that a CPD flux density scales linearly with the Hill radius of the planet, we would expect, following Equation (2):

$$F_{\rm CPD} \propto \left(\frac{a_{\rm p}}{d}\right)^2 \left(\frac{M_{\rm p}}{M_*}\right)^{2/3} B_\nu(T)\cos i, \quad (3)$$

with $a_{\rm p}$ and $M_{\rm p}$ being the orbital radius and mass of the planet, respectively. Adopting a Band 7 flux density for PDS 70 c of $111 \pm 12\,\mu$Jy, computed as the weighted average of the measurements reported by D. Fasano et al. (2025), assuming the same CPD temperature for the two systems, and noting that the two circumstellar disks have similar inclinations, we obtain

$$\frac{F_{\rm WISPIT\ 2b}}{200\ \mu{\rm Jy}} \sim \left(\frac{M_{\rm WISPIT\ 2b}}{M_{\rm PDS\ 70c}}\right)^{2/3}, \quad (4)$$

which suggests that, given the similar estimated planet masses in the two systems, millimeter emission colocated with WISPIT 2b should already be detectable. More detailed modeling, beyond the scope of this Letter, is required to assess whether physically motivated temperatures across the range of plausible planetary masses (for which systematic uncertainties are substantial in both cases) would modify this conclusion.

Under the optically thin assumption, for which the CPD flux density scales linearly with CPD dust mass, our 5σ upper limit of $0.009\,M_\oplus$ on the CPD of WISPIT 2b (assuming 1 mm grains) is comparable to the inferred CPD mass of PDS 70 c, $0.008\,M_\oplus$, derived using the same methodology (rescaling the value of M. Benisty et al. 2021, to account for the different flux density of PDS 70 c used in this Letter). The two planets exhibit similar accretion rates of $\dot{M}_{\rm p} \sim 2 \times 10^{-12}\,M_\odot\ {\rm yr}^{-1}$ (L. M. Close et al. 2025a, 2025b). However, given the large systematic uncertainties in estimates of accretion rates and the intrinsic variability of the Hα line used to determine the accretion on the planets (e.g., L. M. Close et al. 2025b; Y. Zhou et al. 2025), we cannot assess whether a significant difference exists in the CPD accretion timescale $t_{\rm acc} = M_{\rm CPD}/\dot{M}_{\rm p}$. At present, WISPIT 2b remains consistent with the estimates for PDS 70 c, with $t_{\rm acc} \sim 1.2$ Myr when assuming a gas-to-dust ratio of 100.

4.3. Comparison with SPHERE Data

The single narrow ring observed in the millimeter continuum is in stark contrast to the gap-punctuated morphology traced by polarized scattered light (R. F. van Capelleveen et al. 2025). Intriguingly, four concentric rings in the scattered light were observed between 38 and 316 au, while only a single ring was found in the millimeter continuum at 144 au, as shown in Figure 1. A clear result from this simple comparison is that large grains (as traced by ALMA) are predominantly confined at large orbital separation, due to trapping of particles in a local pressure maximum. Smaller grains, as traced by IR scattered light from H to L' bands (L. M. Close et al. 2025a; R. F. van Capelleveen et al. 2025), must be well dynamically coupled to the gas and can be advected radially (see discussion by J. Bae et al. 2019; P. Pinilla et al. 2024, for the PDS 70 system). This configuration clearly shows that, not surprisingly, massive embedded planets are able to trap large particles in confined regions, and lead to the formation of wide cavities at millimeter wavelengths, as predicted by hydrodynamical modeling.

4.4. An Additional Planet beyond WISPIT 2b?

One of the most striking features is the position of WISPIT 2b relative to the edge of the millimeter cavity edge. Theoretical models have shown that the width of the gap opened by a planet (assuming a circular orbit) depends on its mass (e.g., K. D. Kanagawa et al. 2016; S. Zhang et al. 2018). However, for WISPIT 2b the distance to the cavity edge, $\sim$90 au, would require a planet mass that is larger than inferred from infrared photometry. To illustrate this point, Figure 5 displays the width of the millimeter continuum gap normalized to its location as a function of the planet-to-star mass ratio for all detected sources (PDS 70 b and c and WISPIT 2b, shown in color) and putative planets proposed to explain the observed continuum structure (shown as gray points). When a planet is detected, as is the case for PDS 70 b and c and WISPIT 2b, the orbital radius of the planet ($a_{\rm p}$) is used, rather than the gap radius (see caption of Figure 5). Overlaid are two analytical relationships obtained from hydrodynamical simulations by G. P. Rosotti et al. (2016) and S. Facchini et al. (2018) in two different regimes of planet mass, but which show consistent scalings with planet masses.

For a majority of cases, including PDS 70 c, the gap size normalized to the gap location closely follows the expected semianalytical trend. This should not surprise with the nondetections, since the putative protoplanet masses were estimated from a grid of hydrodynamical simulations similar to the ones used to extract the analytical trends shown in Figure 5. PDS 70 b is a clear outlier. Its mass is too low to explain the very wide (sub)millimeter cavity it was detected in, which led to the prediction of another massive companion within the cavity (M. Keppler et al. 2019), later confirmed by the detection of PDS 70 c (S. Y. Haffert et al. 2019). PDS 70 c perfectly matches the expected gap width for its mass. We speculate that WISPIT 2b may be in a similar situation to PDS 70 b: the planet is located too far from our newly detected (sub)millimeter ring for its estimated mass of $4.9\,M_{\rm Jup}$.

This discrepancy could be explained in four ways. The most tantalizing one is that, as in the case of PDS 70 b, another companion is present between WISPIT 2b and the (sub) millimeter ring. The natural location for this planet to reside is the gap in scattered light detected by R. F. van Capelleveen et al. (2025) at about 130 au, yielding $(R_{\rm mm} - R_{\rm gap})/R_{\rm gap} \sim 0.1$. Assuming this semimajor axis, a companion of sub-Jupiter mass follows the relationship predicted by the numerical simulations of S. Facchini et al. (2018) and generates a millimeter ring at 144 au. If located at the inner edge of the scattered-light gap, at about 122 au, such a companion would be in 3:1 mean motion resonance with WISPIT 2b, although simulations will be needed to assess the dynamical stability of the system since this is a second-order resonance.

Alternatively, WISPIT 2b could be on an eccentric orbit, a hypothesis that needs to be reassessed in the light of better orbital characterization of the companion. Current astrometric constraints by R. F. van Capelleveen et al. (2025) indicate that

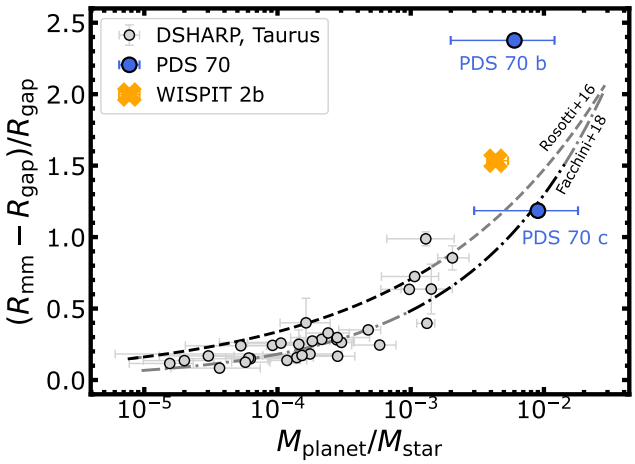

Figure 5. Gap width (in units of the gap radius) as a function of the planet-to-star mass ratio. For systems hosting detected protoplanets, $R_{gap} = a_p$, where a_p is the orbital radius of the planet. The candidate protoplanets in (some of) the gaps in the DSHARP sample (S. M. Andrews et al. 2018; J. Huang et al. 2018) and the Taurus survey of F. Long et al. (2018) are displayed as gray dots, with putative planet masses estimated by A. Ruzza et al. (2025) and stellar masses by S. M. Andrews et al. (2018) and F. Long et al. (2019). PDS 70 b and c are overplotted in blue and WISPIT 2b in yellow. The dashed and dashed–dotted black lines are the expected trends of gap width with planet mass predicted by G. P. Rosotti et al. (2016) and S. Facchini et al. (2018); their extrapolation to the whole range of planet masses we considered is shown in gray.

the eccentricity of the planet's orbit should be $\lesssim$0.3. For a moderately large eccentricity of 0.2–0.3, numerical simulations show that the outer peak in pressure can be located 10%–20% further away from the planet than that around a planet on a circular orbit (private communication; Jaehan Bae). Thus, the high end of the allowed eccentricity range may be able to reconcile the size of the millimeter cavity and the planet masses estimated from IR photometry without an additional outer planet. Analysis of the gas kinematics will be able to reveal dynamical perturbations associated with eccentric planetary orbits (e.g., C. Baruteau et al. 2021).

Another option is that WISPIT 2b could be more massive than inferred by R. F. van Capelleveen et al. (2025) and L. M. Close et al. (2025a) from H- and L'-band photometry, respectively, from 10 up to 15 M_{Jup}, to be consistent with the wide (sub)millimeter continuum cavity. In this case, the gap in scattered light external to WISPIT 2b could be due to shadowing from the ring immediately inwards of it, due to a puffed-up gap edge, as seen in three-dimensional hydrodynamical simulations (e.g., J. Bi et al. 2021). A 15 M_{Jup} planet would also perfectly match the prediction of the ratio between R_{mm} and the IR wall (R_{wall}) outside the planet's orbit as seen in scattered light. From Figure 18 of R. F. van Capelleveen et al. (2025), we can estimate the radius of the IR wall just outside the orbit of WISPIT 2b to be ∼80 au. Inverting equation (1) of M. de Juan Ovelar et al. (2013), which presents the scaling of the radial separation of R_{wall} and R_{mm} with planet mass from a set of hydrodynamical simulations, a ratio $R_{wall}/R_{mm} \sim 0.55$ would require a 15 M_{Jup} planet. However, the gap in scattered light where WISPIT 2b resides would be too narrow to host such a massive planet, according to the predictions of K. D. Kanagawa et al. (2016), and would require extremely high local diffusivities ($\alpha \approx$ a few 10^{-3} up to 10^{-2}) to be consistent with those of S. Zhang et al. (2018). Moreover, in order to reconcile the high planet mass with the IR photometry, we would need to invoke either some extinction along the line of sight to the planet or a cold-start scenario for its evolutionary path. However, such a high-mass planet would induce strong eccentricity in the disk gas. These strong perturbations are not seen in the well-coupled small grains traced by the IR scattered-light images by R. F. van Capelleveen et al. (2025). An analysis of the gas kinematics will promptly reveal any strong eccentric motions in the disk (e.g., I.-H. G. Kuo et al. 2022; J. Calcino et al. 2024; E. Ragusa et al. 2024) and therefore confirm or reject this hypothesis.

Lastly, our scalings of $(R_{mm} - a_p)/a_p$ and R_{wall}/R_{mm} may be biased by the use of two-dimensional, locally isothermal hydrodynamical simulations. A full three-dimensional treatment, with a less simplistic approach for the disk thermodynamics, may present slightly different scaling laws. However, A. J. Cordwell et al. (2025) demonstrated that the observed $(R_{mm} - R_{gap})/R_{gap}$ values in disks require planets more massive than those inferred from 2D simulations and therefore do not alleviate this tension. Dedicated hydrodynamical simulations of the WISPIT 2 system are needed to fully assess this.

As a final note, we stress that the above conclusions are, to some extent, still dependent on the currently available estimates of stellar mass. If in favor of a more massive central star, future accurate estimates (e.g., from disk dynamics) could hasten the discrepancy between WISPIT 2b's mass and the trends in gap width displayed in Figure 5, thus strengthening our hypothesis that an external companion might be present in the system.

5. Conclusions

In this Letter, we analyzed new high-resolution ALMA data of the WISPIT 2 system, the second disk known to unambiguously host an embedded protoplanet (L. M. Close et al. 2025a; R. F. van Capelleveen et al. 2025), that were obtained to search for evidence of circumplanetary emission and to map the distribution of large grains, offering a midplane comparison to the surface structure traced in scattered light. The conclusions of this study are the following:

1. The millimeter thermal emission shows a single, radially resolved, thin (0.″054 or 7.2 au) ring peaking at 1.″086 (144.4 au), far beyond the location of WISPIT 2b (57 au).
2. The radial separation of WISPIT 2b and the millimeter continuum ring is substantially larger than numerical models predict for a 5 M_{Jup} planet. Assuming the photometrically derived mass is robust, this implies that a second, lower-mass planet lies between WISPIT 2b and the millimeter ring, analogous to the PDS 70 system. A natural location of this additional outer planet is the gap detected in scattered light at ∼130 au. Alternatively, WISPIT 2b may occupy a moderately eccentric orbit.
3. Another possibility is that WISPIT 2b is more massive than estimated by IR photometry. Reconciling such a higher mass (>10 M_{Jup}) would require some level of extinction toward the planet. In this scenario, gas kinematic observations should reveal clear signatures of orbital eccentricity.
4. No millimeter emission is detected within the cavity. Injection-and-recovery tests demonstrate that point-source emission at the location of WISPIT 2b above ∼45 μJy can be ruled out at the 3σ level. This excludes the possibility that a potential CPD for WISPIT 2b shows

optically thick continuum emission within one-third of the Hill radius of the planet.

5. The nondetection of a CPD at the location of WISPIT 2b is consistent with the extrapolation of empirical relationships of millimeter flux densities against host mass from the stellar mass regime. Assuming similar temperatures for PDS 70 c and WISPIT 2b, however, we can exclude that the two CPDs follow the same scaling with the planet's Hill radius.

Taken together, these results highlight the power of combining millimeter continuum imaging with complementary shorter-wavelength observations in systems that host embedded protoplanets. Such multiwavelength studies uniquely probe both the disk midplane and surface layers, enabling stringent tests of theoretical models of planet–disk interactions, gap opening, and dust trapping. They also provide crucial empirical constraints on the conditions under which circumplanetary disks may form, and thereby offer an essential pathway toward linking observed protoplanets to their expected formation and accretion environments. Upcoming and future observations of the gas dynamics and hydrodynamical models of WISPIT 2 will further constrain and benchmark the coevolution of protoplanets and their host protoplanetary disk.

Acknowledgments

The authors thank the ALMA Director for awarding time to this DDT program, and the referee for their constructive comments. They are also grateful to Alessandro Ruzza and Andrew Winter for insightful discussions. This Letter makes use of the following ALMA data: ADS/JAO.ALMA 2024.A.00064.S.

ALMA is a partnership of ESO (representing its member states), NSF (USA) and NINS (Japan), together with NRC (Canada), MOST and ASIAA (Taiwan), and KASI (Republic of Korea), in cooperation with the Republic of Chile. The Joint ALMA Observatory is operated by ESO, AUI/NRAO and NAOJ. S.F. acknowledges financial contributions from the European Union (ERC, UNVEIL, 101076613) and from PRIN-MUR 2022YP5ACE. P.C. acknowledges support by the ANID BASAL project FB210003. M.B. has received funding from the European Research Council (ERC) under the European Union's Horizon 2020 research and innovation program (PROTOPLANETS, grant agreement No. 101002188). Views and opinions expressed are however those of the authors only and do not necessarily reflect those of the European Union or the European Research Council. Neither the European Union nor the granting authority can be held responsible for them. This work has been carried out within the framework of the NCCR PlanetS supported by the Swiss National Science Foundation under grant 51NF40_205606. This work made use of the Geryon cluster at the Centro de Astro-Ingenieria UC, which is supported by ANID BASAL project FB21000, BASAL CATA PFB-06, Anillo ACT-86, FONDEQUIP AIC-57, and QUIMAL 130008.

Facility: ALMA.

Software:
`CASA` v6.6.4 (B. Bean et al. 2022), `numpy` (C. R. Harris et al. 2020), `matplotlib` (J. D. Hunter 2007), `galario` (M. Tazzari et al. 2018), `emcee` (D. Foreman-Mackey et al. 2013).

Appendix A
Azimuthally Averaged Visibilities of WISPIT 2

Figure 6 shows the azimuthally averaged visibilities, after deprojection and recentering, with the best-fit `galario` model overplotted on the data. The marginalized posterior distributions of the `galario` fitting procedure are shown in Figure 7.

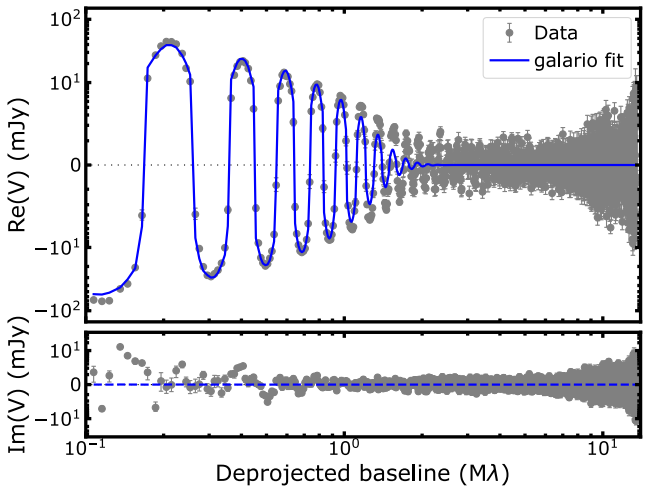

Figure 6. Azimuthal average of the real and imaginary parts of the visibilities after deprojection and recentering, using the best-fit geometrical parameters from the `galario` model, which is shown in blue. Spatial filtering is clear given the large shortest baseline available with these data.

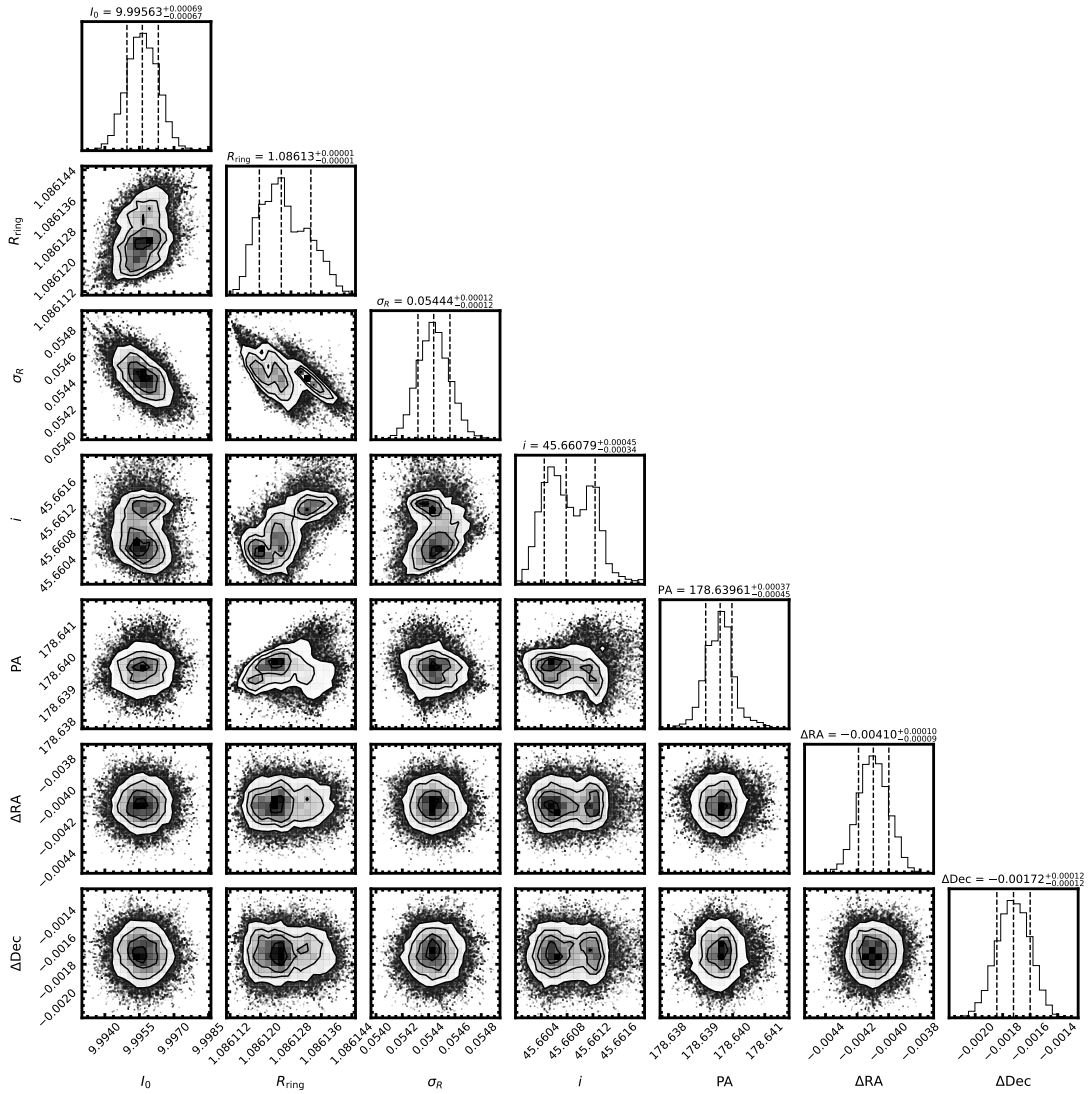

Figure 7. Marginalized posterior distribution of the seven parameters identifying the parametric `galario` model.

Appendix B
Injection–Recovery of a Point Source at the Location of WISPIT 2b and CC 1

We show reconstructed images of a CPD injected at the location of WISPIT 2b, using our default imaging parameters, in Figure 8, for a range of injected flux densities. In Figure 9 we reconstruct the scaling of the rms within the WISPIT 2 millimeter cavity as a function of the resulting `CLEAN` beam, when progressively increasing the angular scale of *uv*-tapering in the imaging.

Finally, we report the results of the injection–recovery of a point source at the location of CC 1 in Figure 10.

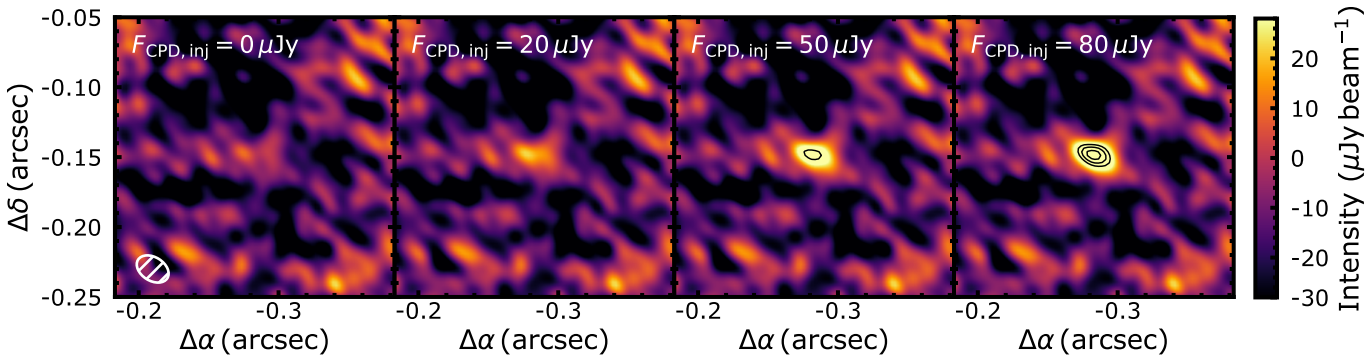

Figure 8. Examples of reconstructed images of a point source injected at the location of WISPIT 2b, located at the center of each frame, after subtracting the best-fit `galario` model in the outer regions (not visible on these angular scales). The coordinates are relative to the center of the ALMA ring. Black contours indicate the [3, 4, 5]σ levels. The `CLEAN` beam is shown in the bottom left of the first panel.

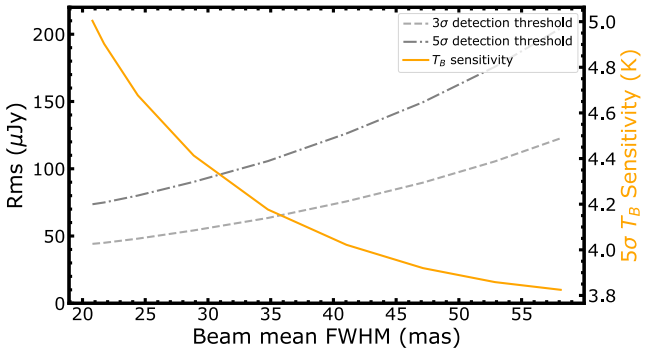

Figure 9. rms estimated within the cavity of WISPIT 2b after removing the best-fit `galario` model, for a large set of imaging parameters, starting from Briggs weighting with `robust` = 1.0, and progressively increasing additional *uv*-tapering ([5, 10, 15, 20, 25, 30, 35, 40] mas). The orange line (portrayed against the *y*-axis on the right side of the panel) shows the 5σ sensitivity of the brightness temperature using the full Planck law.

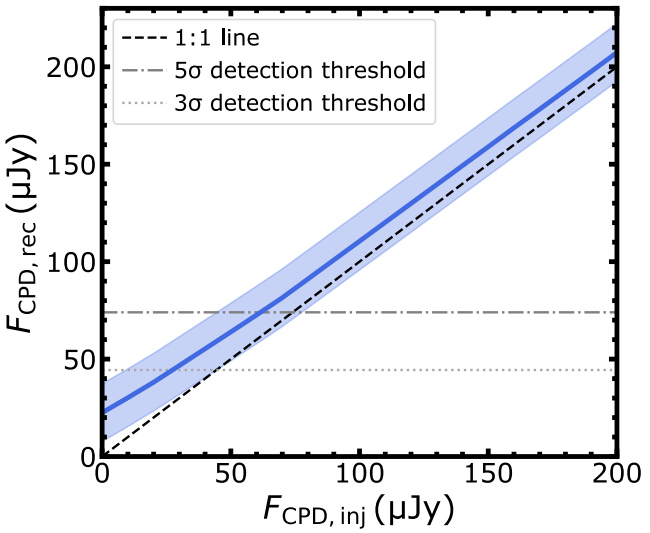

Figure 10. Injected ($F_{CPD,inj}$) versus recovered ($F_{CPD,rec}$) flux density of a point source at the location of CC 1. The legend is the same as for Figure 3.

ORCID iDs

Stefano Facchini https://orcid.org/0000-0003-4689-2684
Pietro Curone https://orcid.org/0000-0003-2045-2154
Myriam Benisty https://orcid.org/0000-0002-7695-7605
Francesco Zagaria https://orcid.org/0000-0001-6417-7380
Richard Teague https://orcid.org/0000-0003-1534-5186
Gabriele Cugno https://orcid.org/0000-0001-7255-3251
Jaehan Bae https://orcid.org/0000-0001-7258-770X

References

Andrews, S. M. 2020, ARA&A, 58, 483
Andrews, S. M., Elder, W., Zhang, S., et al. 2021, ApJ, 916, 51
Andrews, S. M., Huang, J., Pérez, L. M., et al. 2018, ApJ, 869, L41
Aoyama, Y., Ikoma, M., & Tanigawa, T. 2018, ApJ, 866, 84
Ayliffe, B. A., & Bate, M. R. 2009, MNRAS, 397, 657
Bae, J., Isella, A., Zhu, Z., et al. 2023, ASPC, 534, 423
Bae, J., Zhu, Z., Baruteau, C., et al. 2019, ApJL, 884, L41
Baruteau, C., Wafflard-Fernandez, G., Le Gal, R., et al. 2021, MNRAS, 505, 359
Batygin, K., & Morbidelli, A. 2020, ApJ, 894, 143
Bayo, A., Joergens, V., Liu, Y., et al. 2017, ApJL, 841, L11
Bean, B., Bhatnagar, S., Castro, S., et al. 2022, PASP, 134, 114501
Benisty, M., Bae, J., Facchini, S., et al. 2021, ApJL, 916, L2
Benisty, M., Dominik, C., Follette, K., et al. 2023, ASPC, 534, 605
Bi, J., Lin, M.-K., Dong, R., et al. 2021, ApJ, 912, 107
Birnstiel, T., Dullemond, C. P., Zhu, Z., et al. 2018, ApJL, 869, L45
Bowler, B. P., Andrews, S. M., Kraus, A. L., et al. 2015, ApJL, 805, L17
Calcino, J., Norfolk, B. J., Price, D. J., et al. 2024, MNRAS, 534, 2904
Close, L. M., Males, J. R., Li, J., et al. 2025b, AJ, 169, 35
Close, L. M., van Capelleveen, R. F., Weible, G., et al. 2025a, ApJL, 990, L9
Cordwell, A. J., Ziampras, A., Brown, J. J., & Rafikov, R. R. 2025, MNRAS, 543, 4198
Cugno, G., Facchini, S., Alarcon, F., et al. 2025, AJ, 170, 317
Cugno, G., Pearce, T. D., Launhardt, R., et al. 2023, A&A, 669, A145
de Juan Ovelar, M., Min, M., Dominik, C., et al. 2013, A&A, 560, A111
Domínguez-Jamett, O., Casassus, S., Baobab Liu, H., et al. 2025, A&A, 702, A18
Facchini, S., Pinilla, P., van Dishoeck, E. F., & de Juan Ovelar, M. 2018, A&A, 612, A104
Fasano, D., Benisty, M., Curone, P., et al. 2025, A&A, 699, A373
Foreman-Mackey, D., Hogg, D. W., Lang, D., & Goodman, J. 2013, PASP, 125, 306
Haffert, S. Y., Bohn, A. J., de Boer, J., et al. 2019, NatAs, 3, 749
Harris, C. R., Millman, K. J., van der Walt, S. J., et al. 2020, Natur, 585, 357
Huang, J., Andrews, S. M., Pérez, L. M., et al. 2018, ApJL, 869, L43
Huélamo, N., Chauvin, G., Mendigutía, I., et al. 2022, A&A, 668, A138
Hunter, J. D. 2007, CSE, 9, 3
Isella, A., Benisty, M., Teague, R., et al. 2019, ApJL, 879, L25
Kanagawa, K. D., Muto, T., Tanaka, H., et al. 2016, PASJ, 68, 43
Kelly, B. C. 2007, ApJ, 665, 1489
Keppler, M., Benisty, M., Müller, A., et al. 2018, A&A, 617, A44
Keppler, M., Teague, R., Bae, J., et al. 2019, A&A, 625, A118
Kuo, I.-H. G., Yen, H.-W., Gu, P.-G., & Chang, T.-E. 2022, ApJ, 938, 50
Lega, E., Benisty, M., Cridland, A., et al. 2024, A&A, 690, A183
Long, F., Herczeg, P., Harsono, G. J., et al. 2019, ApJ, 882, 49
Long, F., Pinilla, P., Herczeg, G. J., et al. 2018, ApJ, 869, 17
MacGregor, M. A., Wilner, D. J., Czekala, I., et al. 2017, ApJ, 835, 17

Manara, C. F., Ansdell, M., Rosotti, G. P., et al. 2023, ASPC, 534, 539
Marleau, G.-D., Kuiper, R., Béthune, W., & Mordasini, C. 2023, ApJ, 952, 89
Pinilla, P., Benisty, M., & Birnstiel, T. 2012, A&A, 545, A81
Pinilla, P., Benisty, M., Waters, R., Bae, J., & Facchini, S. 2024, A&A, 686, A135
Ragusa, E., Lynch, E., Laibe, G., Longarini, C., & Ceppi, S. 2024, A&A, 686, A264
Ren, B. B., Benisty, M., Ginski, C., et al. 2023, A&A, 680, A114
Ricci, L., Cazzoletti, P., Czekala, I., et al. 2017, AJ, 154, 24
Rosotti, G. P., Juhasz, A., Booth, R. A., & Clarke, C. J. 2016, MNRAS, 459, 2790
Ruzza, A., Lodato, G., Rosotti, G. P., & Armitage, P. J. 2025, A&A, 700, A190
Tazzari, M., Beaujean, F., & Testi, L. 2018, MNRAS, 476, 4527
Trevascus, D., Blunt, S., Christiaens, V., et al. 2025, A&A, 698, A19
van Capelleveen, R. F., Ginski, C., Kenworthy, M. A., et al. 2025, ApJL, 990, L8
van der Marel, N. 2023, EPJP, 138, 225
Wang, J. J., Ginzburg, S., Ren, B., et al. 2020, AJ, 159, 263
Wu, Y.-L., Bowler, B. P., Sheehan, P. D., et al. 2020, AJ, 159, 229
Wu, Y.-L., Bowler, B. P., Sheehan, P. D., et al. 2022, ApJL, 930, L3
Zhang, S., Zhu, Z., Huang, J., et al. 2018, ApJL, 869, L47
Zhou, Y., Bowler, B. P., Sanghi, A., et al. 2025, ApJL, 980, L39